

Interactions of Human Endothelial Cells with Gold Nanoparticles of Different Morphologies

Dorota Bartczak, Otto L. Muskens, Simone Nitti, Tilman Sanchez-Elsner, Timothy M. Millar, and Antonios G. Kanaras*

The interactions between noncancerous, primary endothelial cells and gold nanoparticles with different morphologies but the same ligand capping are investigated. The endothelial cells are incubated with gold nanospheres, nanorods, hollow gold spheres, and core/shell silica/gold nanocrystals, which are coated with monocarboxy (1-mercaptopundec-11-yl) hexaethylene glycol (OEG). Cell viability studies show that all types of gold particles are noncytotoxic. The number of particles taken up by the cells is estimated using inductively coupled plasma (ICP), and are found to differ depending on particle morphology. The above results are discussed with respect to heating efficiency. Using experimental data reported earlier and theoretical model calculations which take into account the physical properties and distribution of particles in the cellular microenvironment, it is found that collective heating effects of several cells loaded with nanoparticles must be included to explain the observed viability of the endothelial cells.

1. Introduction

The use of advanced nanomaterials in biomedicine is a rapidly emerging area of research.^[1–4] The unique properties of engineered colloidal nanoparticles, equipped with a toolkit of functionalities, open up a wide range of applications in imaging and theranostics.^[5,6] For example, different types of nanoparticles can serve as contrast agents for long-term tracking of biomolecules,^[7–9] carriers for targeted and efficient drug delivery,^[10,11] probes for the manipulation of cellular functions,^[12,13] and agents

for laser-induced nanosurgery and cancer treatment.^[14–18] In order to develop such advanced applications, the interactions of nanoparticles with biological systems have to be understood at a fundamental level. Important questions that must be answered relate to a) how the nanoparticle characteristics (morphology, functionality, and chemical composition) and the degree of nanoparticle agglomeration influence their uptake and distribution within different types of cells; b) what is the cytotoxicity of the different types of nanoparticles taken up by the cells; and c) how the cellular behavior is affected by nanoparticles. Studies addressing these important topics will help to choose the most appropriate and efficient types of nanoparticles for imaging, sensing, therapy, and drug delivery.

An increasing number of reports have appeared in recent years where the authors have studied the interactions of semiconductor, metal oxide, and metallic nanoparticles with biological systems.^[19–25] Amongst these types of particles, gold nanoparticles (GNPs) have been shown to be particularly attractive. Gold nanoparticles exhibit relatively good biocompatibility and low toxicity in comparison to other kinds of inorganic nanoparticles (e.g., cadmium-based quantum dots), as well as high affinity towards amine- and thiol-containing biomolecules. Moreover, several types of GNPs (e.g., rodlike, hollow gold, silica/gold core/shell) show strong optical resonances in

Dr. D. Bartczak, Dr. O. L. Muskens, Dr. A. G. Kanaras
School of Physics and Astronomy
University of Southampton
Southampton, SO171BJ, UK
E-mail: a.kanaras@soton.ac.uk

Dr. T. Sanchez-Elsner, Dr. T. M. Millar
School of Medicine
University of Southampton
Southampton, SO16 6YD, UK

S. Nitti
Istituto Italiano di Tecnologia
Via Morego 30, 16163 Genova, Italy

DOI: 10.1002/sml.201101422

the near-IR range of the spectrum, offering the opportunity for application of these particles in imaging and phototherapy.^[1,17,26]

Several studies have recently investigated the cellular uptake of GNPs of various morphologies and functionalities.^[27–33] Chan and co-workers reported that citrate coated spherical and rodlike GNPs were both endocytosed by HeLa cells with spherical GNPs taken-up more efficiently than rodlike NPs.^[34] It was demonstrated that the uptake rate of spherical citrate-coated GNPs of 50 nm diameter was higher than for particles of 14 or 74 nm. In another report from the same group 14 nm transferrin-coated GNPs were exocytosed quicker than larger particles of diameters up to 100 nm.^[35] Stellacci and co-workers reported that 5–6 nm gold NPs capped with a mixed layer of hydrophobic and anionic ligands arranged in ribbon-like domains, could penetrate the cellular membrane of dendritic cells without disrupting it whereas GNPs with identical hydrophobic content but in the absence of structurally organized ligands were taken-up by cells and trapped within endosomes.^[36] Rotello and co-workers also showed that particles of different charges can migrate in different locations within tumor cylindroids.^[37]

Despite the significant number of studies focused on the interaction of GNPs and cells, as highlighted in several recent reviews,^[38–40] the general understanding of the interactions between nanoparticles and cells remains limited. This is due to the inherent complexity resulting from a large variety of different nanoparticle and cell types, as well as to the intrinsic variation of experimental conditions. Moreover, many reports focus on cancer cell lines, which differ substantially from non-cancerous cell types.

Endothelial cells line the entire circulatory system, from the heart to the smallest capillary, assemble the blood–brain barrier of an organism and are involved in the growth and metastasis of cancer. As such, they are an important type of mammalian cells. Here, we present for first time a study of the interactions between GNPs of four different morphologies, but of the same ligand capping, with noncancerous, primary human endothelial cells. We specifically discuss how different morphologies influence the cellular uptake of nanoparticles, their cytotoxicity, and the laser-induced cell death. Our studies provide a better understanding which aids the selection of the most appropriate types of particles for applications including drug delivery inside the cell and laser treatment, especially when the cellular micro-environment near a tumor site has to be considered.

2. Results and Discussion

We have employed four types of morphologically different GNPs: spherical (SP), rodlike (NR), hollow gold (HG) and core/shell silica/gold (CS). **Figure 1** shows transmission

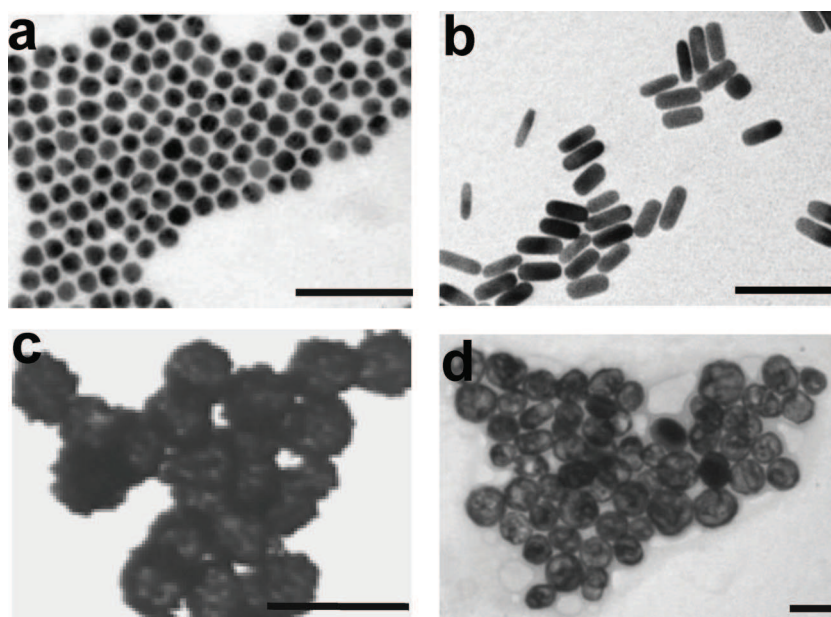


Figure 1. TEM images of various types of gold nanoparticles: a) gold nanospheres, b) gold nanorods, c) silica/gold core/shell nanoparticles, and d) hollow gold nanoparticles. Scale bars are 100 nm.

electron microscopy (TEM) images of all the different types of nanoparticles. Analyzing a large set of TEM images (see Supporting Information (SI) for histograms) we estimated the average size of each type of particles, as shown in **Figure 2**. All GNPs were stabilized with monocarboxy (1-mercaptopundec-11-yl) hexaethylene glycol (OEG). As previously reported,^[20,41,42] the OEG capping layer enhances the stability of NPs against aggregation and minimizes the possibility of nonspecific interactions with biological molecules such as serum proteins. Moreover, the negative charge of the OEG GNPs reduces their possible cellular toxicity, whereas the ethylene glycol units may increase the retention times of the particles in the blood.^[43] The nanoparticles were characterized with several techniques including UV–visible spectroscopy (see SI), TEM, dynamic light scattering (DLS), and zeta potential measurements. The nanoparticles were robust in solution and did not show any signs of aggregation.

As expected, the zeta potential measurements indicated a strong negative charge for all the types of OEG GNPs. The smallest OEG SP had the lowest net charge (-28 ± 2 mV), while the largest OEG HG had the highest (-40 ± 2 mV). The average number of OEGs attached to each nanoparticle was estimated with Ellman's method.^[44] At least ten independent measurements were performed for each type of NP, the summary of which is shown in **Figure 2**. In all cases the number of capping ligands was sufficient to provide the appropriate surface stabilization. As expected, the larger particles (HG) have the highest number of OEG ligands ($\approx 55\,871$), while the smallest (SP) have the lowest number (≈ 1876).

2.1. Cellular Uptake of OEG GNPs

The cellular uptake of the different types of nanoparticles was studied using TEM and inductively coupled plasma-atomic

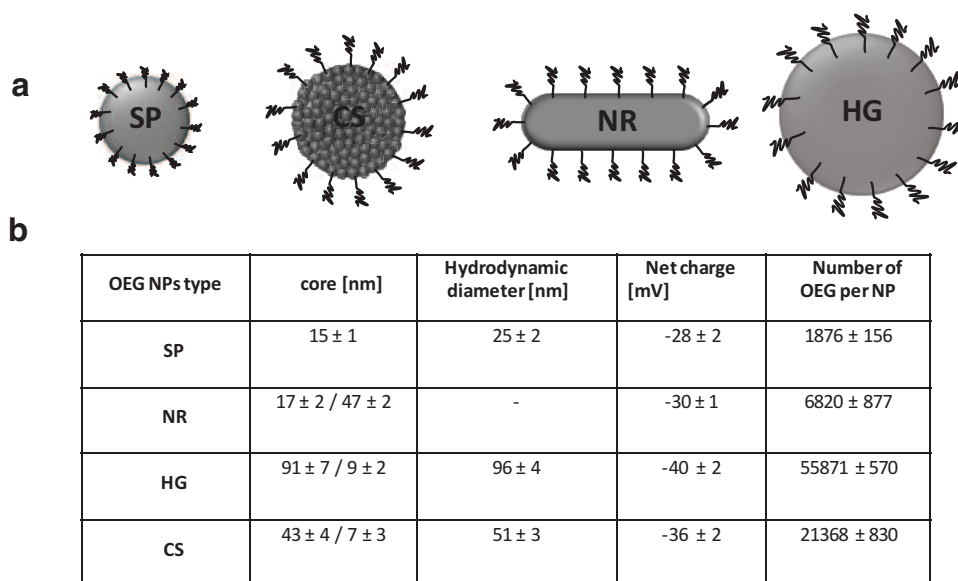


Figure 2. a) Schematic illustration of OEG-coated gold nanoparticles. b) Physicochemical characterization of OEG-capped gold nanoparticles of different morphologies. The hydrodynamic diameter, zeta potential, and average number of ligands per particle is shown.

emission spectroscopy (ICP-AES). **Figure 3** shows TEM images of cross-sectioned endothelial cells incubated with OEG GNPs. The images show that the GNPs were internalized by the endothelial cells, and were found confined within intracellular vesicles. In most cases, the well-preserved double membrane

of the vesicles can be easily distinguished (see Figure 3a and SI), which suggests endocytosis as the most probable pathway of internalization. As can be seen in Figure 3d (and SI) the orientation of gold nanorods within vesicles is random. Some nanorods are aligned horizontally to the TEM grid and appear

as elongated structures on the image, while others are lined up vertically in the 100 nm-thick cellular section, giving the impression of a more spherical shape. In most images, the GNPs assembled in the vesicles are found to consist of collections of 10–100 particles. This observation is of importance for its consequence in laser treatments.

The average number of nanoparticles per cell was estimated with ICP. The cells (100 000) were incubated with GNPs (1 mL, 8.3 nM) for 4 h in endothelial growth medium (20% human serum, M199 media, penicillin/streptomycin/glutamine) at 37 °C, 5% CO₂ in a humidified incubator purified and processed for ICP-AES. The results from three independent experiments for all of the different types of particles are shown in Figure 3e. The numbers of particles taken up by the cells were estimated from the total mass of gold, divided by the average mass per particle.

The first observation from Figure 3e is that in our study, particles are taken up in lower numbers compared to other studies on differently functionalized nanoparticles.^[32,34,35] This is probably due to the strong negative charge of the OEG GNPs in conjunction with the ability of the ethylene glycol units to prevent most of the nonspecific interactions between the nanoparticle

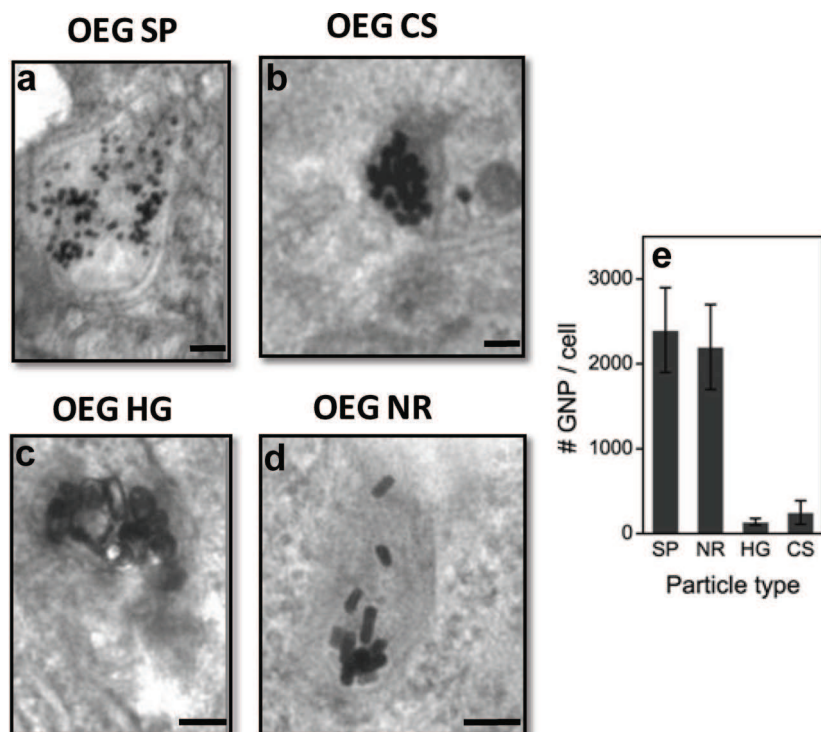


Figure 3. a–d) TEM images of cross-sectioned endothelial cells loaded with OEG-coated gold nanoparticles. a) OEG SPs: spherical gold nanoparticles, b) OEG CS: silica core/gold shell nanoparticles, c) OEG HG: hollow gold nanoparticles, and d) OEG NR: gold nanorods. Scale bars are 100 nm (for lower scale images see SI). e) Average number of particles per endothelial cell obtained from ICP-AES data.

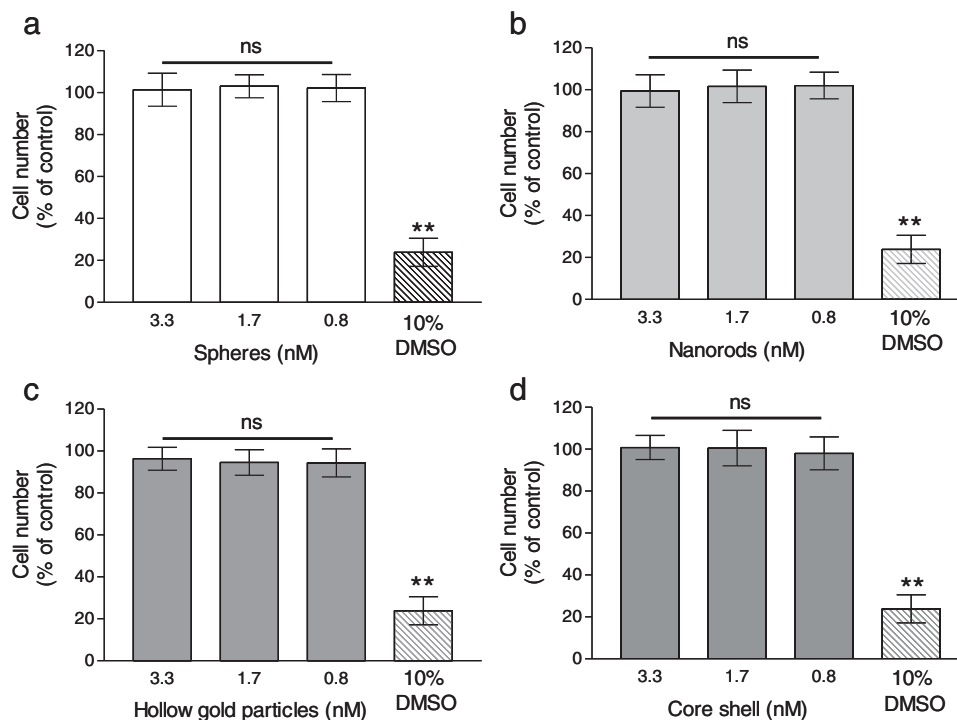


Figure 4. Chronic cytotoxicity profile of endothelial cells when loaded with the different types of particles: a) spheres, b) nanorods, c) hollow gold particles, and d) core/shell silica/gold. The number of alive cells remain the same after 96 h of incubation with the particles in various concentrations. A positive control (10% DMSO) is used for comparison. A t-Test analysis showing the level of significance (p) is indicated as (**) for significant and 'ns' for insignificant values (see SI for calculated values).

surface and proteins or other biomolecules as reported by others.^[33] In our experiments the highly negative HG and CS nanoparticles are found within the cells at the lowest concentrations compared to the other particle types. One could speculate that the stronger negative charge of HG makes it difficult for these particles to physically approach the cells, due to stronger repulsion from the negatively charged cellular membrane of human umbilical vein endothelial cells (HUVECs). However, although the NR are slightly more negative than the SP, they are internalized in larger numbers than the spheres. On the other hand the 50 nm-sized CS particles are taken up in lower numbers than the 100 nm-sized HG. Both of these experimental results deviate from observations made in recent literature regarding size- and shape-dependent uptake in HeLa cells.^[34,35] A possible reason for this discrepancy may be partly explained by a) the type and normal physiology of the cells utilized; primary endothelial cells as opposed to immortalized cervical epithelial cells; b) the nature of surface coating of NPs (charge and type of ligand); and c) the experimental conditions used (i.e., incubation times). These characteristics are equally critical as the size and shape of nanoparticles, and are expected to influence strongly the cellular uptake of GNPs.

2.2. Cytotoxicity of OEG-Capped NPs

One more aspect should not be omitted when investigating the interactions between mammalian cells and NPs: the survival rate of cells transfected with NPs. We have measured the number of endothelial cells after prolonged (in

comparison to cell uptake studies) 96 h treatment with OEG NPs, in respect to untreated cells. Briefly, as endothelial cells have an adherent phenotype and stop dividing once they reach confluence, their numbers are relatively stable. If cells die by apoptosis or necrosis, then they lose adherence and can be removed from the culture by gentle washing. For this reason we are able to assess cytotoxicity by measuring relative cell number compared to untreated cells. This is achieved by labeling the DNA of adherent cells with the DNA specific dye Hoechst 33342 which fluoresces on binding to DNA at 460 nm after being excited at 350 nm. The untreated cells of a 96 well plate with a confluent monolayer of labeled endothelial cells give the maximum fluorescence and are designated as 100% cell number. All other treatments are related to this fluorescence to assess the number of adherent cells. In our experiments, endothelial cells were seeded at 2×10^4 cells per well and grown to confluence in 96 well plates. They were then exposed to either growth medium alone (100% control), various nanoparticles (treatment) or 10% dimethyl sulfoxide (DMSO, positive control causing cell death and detachment from the plates) for 96 h, after which cells were stained with Hoechst 33342 and the number of adherent cells was measured relative to untreated controls. The results from at least three independent experiments are shown in **Figure 4**. No significant effects (see SI for statistical analysis) on the cell number were seen when endothelial cells (ECs) were treated with the different types of OEG NPs. Even doubling the concentration of NPs did not cause chronic toxicity. Also, no differences in the overall cell number were observed when

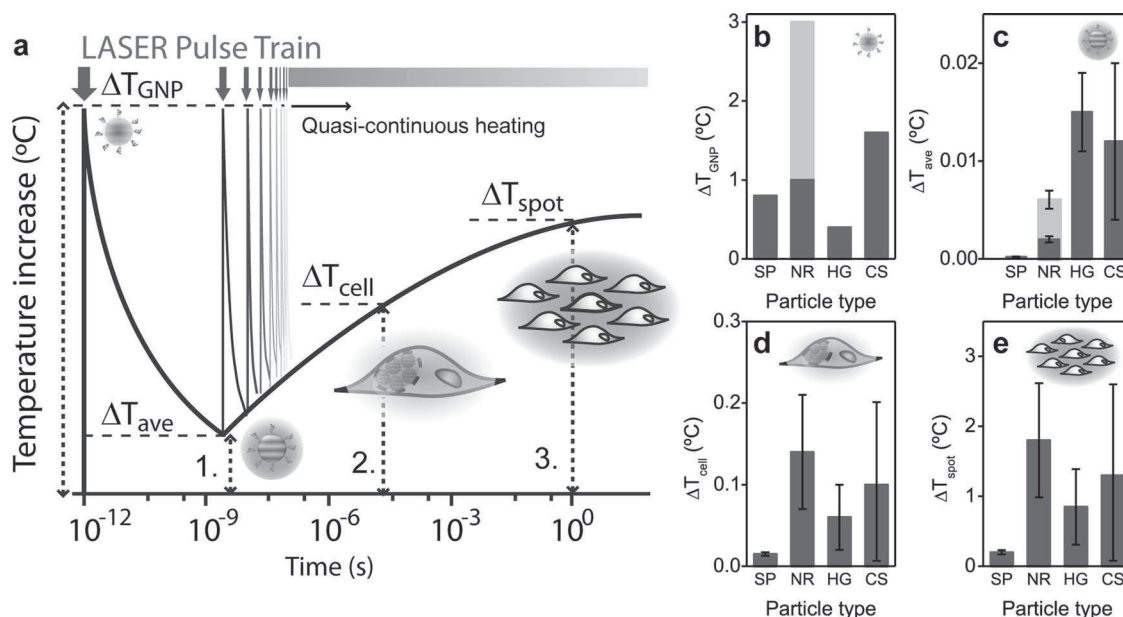


Figure 5. a) Schematic illustration of length scales and time scales in nanoparticle heating, showing the time scales (logarithmic) of pulsed-laser heating of: a single-particle (1), a single cell (2), and of the entire illumination area (3). b–e) Calculated values of: peak temperature ΔT_{GNP} (b); average temperature ΔT_{ave} for a single nanoparticle (c); temperature increase ΔT_{cell} of a cell of 10 μm diameter (d); temperature increase ΔT_{spot} of a 200 μm -diameter illumination area containing 100 cells (e).

reduced concentrations of OEG NPs were used. Consequently, it was concluded that at the concentrations needed in our experiments, transfected ECs remain adherent.

2.3. Implications for Laser-Induced Treatment

In the following, we include the above characterizations of the uptake and distribution of GNPs of various morphologies to assess the possible mechanisms of laser-induced treatment. Recently, we have shown experimentally that low-intensity illumination at a wavelength of 690 ± 10 nm resulted in significant damage of endothelial cells incubated with GNPs.^[14] Here, we combine the information on internalization and clustering of OEG-capped NPs in the endosomes to calculate the local and global heating effects using a simple model of pulsed laser illumination (described in the SI). We assumed a laser intensity of 30 W cm^{-2} which corresponds to the mild hyperthermia conditions used in experiments.^[14] Using these model calculations, we can draw conclusions on the mechanism of laser-induced heating for the OEG NPs and compare these with our experimental results reported earlier for NR, HG, and CS GNPs.^[14] For SPs, we compare the maximum possible heating effect at the SPR maximum (see SI, Figure S1). Nanoparticle heating effects can be distinguished on several different length scales and time scales, as shown in **Figure 5**. Following illumination by a short picosecond-pulsed laser, light absorbed by a nanoparticle results in a short non-equilibrium spike of heat inside the particle characterized by the single-particle temperature rise ΔT_{GNP} (Figure 5b). The peak temperature rise is determined by the absorbed energy divided by the total particle heat capacity, both of which scale with particle volume. A small spherical (SP) GNP has a small

absorption but also a small heat capacity, and therefore shows a peak temperature rise larger than that of a much larger HG particle. The similar scaling of absorption and heat capacity with particle size means that the particle size distribution does not affect the peak temperature, explaining the absence of error bars in Figure 5a. For the gold NR, two temperatures are shown corresponding to random polarization of the incident light (dark grey bar) and polarization parallel to the NR long-axis (light grey bar). Particle orientation plays a role in single-nanoparticle heating as it defines the amount of light that is absorbed through the longitudinal surface plasmon resonance. The peak temperature ΔT_{GNP} is of importance in pulsed-laser treatment as it can trigger nonequilibrium changes of biomolecules attached to the GNPs.^[45]

Following pulsed excitation, the particle temperature rapidly decays within 100 ps through diffusion of heat to the surroundings of the GNP, and only a low average temperature ΔT_{ave} remains (Figure 5c). For a train of short pulses, this average temperature includes the accumulative effect of multiple laser pulses in a single GNP. Clearly, ΔT_{ave} is several orders of magnitude smaller than the peak temperature rise ΔT_{GNP} . The different values of ΔT_{ave} for different types of GNP illustrate the heat-generation capacity of the various particles, which is directly proportional to their absorption cross-section. Error bars in Figure 5c include estimated variation in absorption cross section due to the experimental distribution in particle volume (see SI for histograms).

Clearly, single-nanoparticle heating does not produce a sufficient temperature rise to explain the cell damage observed in experiments at the laser intensities under study. Indeed single-particle heating has been shown to be relevant at 10^4 times higher laser intensities.^[46] Therefore, we calculate also collective heating effects which take place on the level of

an endosome, a whole cell, and the laser illumination spot. On these length scales, the pulsed nature of the illumination does not produce a marked variation in temperature, and we can replace the pulse train with a quasi-continuous energy source, as indicated in Figure 5a. As shown in the SI, even an aggregate containing 100 GNP does not produce a local temperature increase above 1 °C for all particle types and for the illumination conditions under study. The same is true for the temperature rise in a single cell ΔT_{cell} shown in Figure 5d, where we have modeled the cell by a spherical volume containing an amount of GNP as specified in Figure 3. The error bars now reflect both the distribution of particle sizes as well as the uncertainty in the number of GNP per cell. Only on the scale of the 200 μm illumination spot the temperature rise ΔT_{spot} is substantial, i.e., several degrees, as is shown in Figure 5e. This is consistent with macroscopic model studies of nanoparticle photothermal energy conversion in solutions, where temperature changes were found to take place on the time scale of seconds to minutes in a nanoparticle solution.^[47,48]

Remarkably, the large variation in nanoparticle uptake is balanced by the difference in absorption cross section for the NR, CS, and HG, resulting in a similar calculated temperature increase per cell and over the entire illumination spot. In experiments a three times larger percentage of cell death was found for the HG and NR than for the CS.^[14] This trend is not observed in our calculations. Most likely, variations within a factor of 2 are easily obtained through variations in exact GNP properties resulting in different spectral response. This may be more prominent for the CS type of GNP where a small variation in shell thickness and morphology will result in large spectral shifts of the plasmon resonances. Also we note that clustering of GNP inside endosomes will change the absorption spectra of nanoparticles,^[49] resulting in different amounts of absorbed energy.

The combination of our model calculations with our previously reported experimental results^[14] can be used to eliminate several mechanisms of laser-induced treatment. Clearly, heat-generation at the single-particle level is insufficient to produce a large temperature effect. The maximum nonequilibrium temperatures in the GNP reached during pulsed illumination are of the same order as the average thermal effect over the illumination spot. Our results do not address possible nonthermal contributions related to generation of oxidative species, such have been proposed in other work.^[15] In order to explain the cell damage via equilibrium heat generation, one has to go to the macroscopic scale by including collective heating of a monolayer of endothelial cells over several hundred micrometers. This observation is important, as it implicates that this will affect all cells in the illumination volume, limiting the possibility of targeting of individual cell types. Time-resolved calculations of heat diffusion predict that an equilibrium temperature within the illumination area will be reached within a time scale of 0.1 s. Ultimately the temperature increase in the illumination spot will be governed by heat flux into the surrounding medium. The absence of thermal damage outside the treated area in previously reported work by us^[14] shows that this heat flux does not result in a buildup of temperature in the culture beyond the

illumination spot, limiting the equilibrium temperatures to those shown in Figure 5e.

3. Conclusion

Endothelial cells form an important class of cells which constitute several of the most important barriers to nanoparticles inside the body, including vasculature and the blood-brain barrier. We investigated the basic interactions between OEG-coated GNPs and endothelial cells and have addressed the implications for laser treatment of endothelial cells using nanoparticles. We studied four types of OEG-coated nanoparticles (gold nanospheres, nanorods, hollow, and core/shell silica/gold particles) and found that none of these are cytotoxic at various concentrations in our experimental conditions. We showed that the morphological differences among nanoparticles affect their number taken up by endothelial cells. The OEG-coated hollow gold and the core/shell silica/gold particles are taken up the least by endothelial cells. Although the gold nanorods are taken up 100 times more than the hollow gold particles, they are equally efficient in promoting cell death when laser hyperthermia is employed. The latter observation is supported by theoretical calculations. The knowledge of NPs cellular uptake, cytotoxicity and laser treatment implication gathered in this study will be of importance for many applications involving nanoparticle delivery through the endothelium, as well as for nanotechnological manipulation of processes involving vasculature formation (angiogenesis), which will be explored in future studies.

4. Experimental Section

Chemical Synthesis of Nanoparticles: Gold NPs were prepared according to well-established protocols.^[50] Briefly, spherical NPs were prepared by the citrate reduction method and stabilised by bis(p-sulfonatophenyl)phenyl phosphine dehydrate dipotassium salt (BSPP) as previously reported by our group.^[12]

Gold nanorods were synthesized by a seed mediated growth method.^[51] In detail, to a growth solution consisting of: hexadecyltrimethylammonium bromide (CTAB), (0.2 M, 7.12 mL), sodium tetrachloroaurate (III) dehydrate, (5 mM, 2 mL), silver nitrate (5 mM, 0.17 mL) and freshly prepared L-ascorbic acid (0.0788 M, 0.16 mL), 16 μL of gold seeds [prepared by the reduction of gold salt (5 mM, 1 mL) in the presence of CTAB (0.2 M, 1 mL) and sodium borohydride (0.01 M, 0.5 mL)] were added, then shaken gently and left overnight at 35 °C.

Silica/gold core/shell NPs were prepared via a previously reported method.^[52] First, ammonia solution (30%, 3 mL) was added to 50 mL of absolute ethanol, and then tetraethyl orthosilicate (TEOS, 6.7 mmol, 1.5 mL) was added drop-wise, followed by 30 min. stirring. The silica particles were purified by centrifugation (3 \times , 10 000 rpm, 10 min). Then, 3-(aminopropyl) trimethoxysilane (APTMS), (2.8 mmol, 0.5 mL) was added into 50 mL of a vigorously stirred silica NPs solution and allowed to react for 2 h prior to purification by centrifugation. Meanwhile, gold seeds were prepared by mixing sodium hydroxide solution (1 M, 0.5 mL), tetrakis(hydroxymethyl)phosphonium chloride (THPC),

(0.067 mmol, 1 mL) and 45 mL of water, followed by injection of the gold salt (1%, 0.75 mL). Seeds (5 mL) were then mixed with silica/APTMS NPs (0.5 mL in water), allowed to stand for 2 h and purified by centrifugation (3×, 10 000 rpm, 10 min) prior to the shell growth. Seed-APTMS-silica NPs (200 µL) were added to 4 mL of an ice cold growth solution (potassium carbonate (25 mg) in 100 mL of water). Then formaldehyde (0.36 mmol, 10 µL) was injected and the mixture was allowed to react for 5 min.

Hollow gold NPs (HG) were prepared as follows. To a growth solution consisting of: CTAB (0.2 M, 80 mL), silver nitrate (0.05 M, 400 µL) and freshly prepared L-ascorbic acid (0.1 M, 2 mL), 400 µL of silver seed solution (synthesized by the reduction of silver nitrate (2.5 mM, 1 mL) mixed with trisodium citrate (2.5 mM, 1 mL), sodium borohydride (0.001 M, 25 µL), and 8 mL of water) was added. Sodium hydroxide (1 M, 2 mL) was injected to this solution. The mixture was left overnight at 35 °C prior to purification (centrifugation, 3× 10 000 rpm, 10 min). The silver nanoparticles (10 mL) were brought to boil and refluxed for 10 min, followed by a drop-wise addition of gold salt (1 mM, 0.25 mL) and additional 20 min of reflux.

Preparation of OEG-Coated NPs: Freshly prepared OEG (mono-carboxy (1-mercaptoundec-11-yl) hexaethylene glycol) aqueous solution (5 mg mL⁻¹, 200 µL, MW = 526.7) was added to a solution of gold SP (10 mL, 5 nm), while stirring. The mixture was incubated for 2 h at room temperature, then overnight at 4 °C. Capped NPs were purified by three steps of centrifugation/decantation (16 000 rpm, 15 min) and redispersed by sonication in sodium borate buffer (10 mL, 0.01 M, pH 9) prior to physicochemical characterisation or a medium growth (M199, 20% human serum, 1 mL) prior to experiments with cells. NPs were stored at 4 °C.

Anisotropic (NR, HG and CS) gold NPs were capped with OEG ligands as followed. A fresh solution of OEG (5 mg mL⁻¹, 200 µL, MW = 526.7) was injected into an aqueous solution of gold NPs (5 mL; optical density, OD = 0.5), whilst sonicating at 4 °C. This was immediately followed by the addition of sodium borate buffer (5 mL, 0.02 M, pH 9). Gradually over 1 h, the temperature was increased to room temperature, then held at room temperature for 2 h with stirring. This was followed by 30 min of sonication at room temperature and overnight incubation at 4 °C. Capped NPs were purified by three steps of centrifugation/decantation and redispersed by sonication in sodium borate buffer (10 mL, 0.01 M, pH 9) prior to characterisation or a medium growth (1 mL) prior to experiments with cells. NPs were stored at 4 °C.

Supernatants left at each step of purification were combined and stored at 4 °C prior to the quantification of the thiol content, as described in the following section.

Characterization of Nanoparticles: The shape and size of NPs was determined by transmission electron microscopy. UV-visible spectra were measured using a Cary 300 Bio UV-vis spectrophotometer from 400 to 900 nm. The images were obtained with a Hitachi H7000 TEM operating at a bias voltage of 75 kV. The hydrodynamic diameter of OEG NPs and their net charge were measured with a Zetasizer Nano ZS (Malvern Instruments Ltd.).

The number of OEGs per nanoparticle was estimated using the Ellman's thiol quantification method. Briefly, quantification buffer (0.5 mL, 0.1 M sodium phosphate, pH 8; 1 mM ethylenediamine-tetraacetic acid (EDTA)) was mixed with Ellman's reagent (10 µL, of solid 5,5'-dithiobis(2-nitrobenzoic acid) (DTNB) dissolved in 1 mL of quantification buffer). To which, the thiol containing solution (50 µL

of combined supernatants, left after each step of purification; 0.1 ÷ 1 mM range) was introduced and mixed. The reaction mixture was incubated for 15 min at room temperature and the maximum absorbance value was measured at 412 nm. Eventually, the thiol content was calculated from the calibration curve (prepared by measuring a series of dilutions with a given concentration of the quantified thiol, ranging from 0 ÷ 1.5 mM).

HUVEC Isolation and Culturing: HUVECs were harvested from human umbilical veins by collagenase digestion. Umbilical cords and placentas were harvested at term following natural delivery at the Princess Anne Hospital, Southampton, UK following local ethically approved procedures (Ethics submission number: 07/H0502/83). Umbilical cords were typically stored at 4 °C until use, within 24 h of delivery. Cords were perfused with Type 1 collagenase solution (1 mg mL⁻¹, Worthington) for 10 min at 37 °C, before endothelial cells were harvested by centrifugation, then seeded onto T-75 cm flasks. Flasks and subsequent culture plastic were precoated with porcine gelatin (0.2% in Hank's Buffered Salt Solution-HBSS, Sigma-Aldrich). Cells were passaged by trypsin digestion and grown to confluence in M199 (Invitrogen) media containing 20% human serum (Autogen Bioclear) and penicillin/streptomycin (Invitrogen) at 37 °C in a humidified 5% carbon dioxide (CO₂) balanced air incubator. Endothelial lineage was confirmed by cobblestone appearance in culture, by distinct punctate expression of von Willebrand factor (vWF) and by Cluster of Differentiation molecule number 31 (CD31) expressions (data not shown). HUVECs were cultured on porcine gelatin (0.2% in HBSS) precoated culture dishes, in a media growth (M199) containing 20% human serum in 5% CO₂ air balanced incubator at 37 °C. HUVECs only from first or second passage were used in all experiments.

HUVECs were treated with OEG-capped SP, NR, HG, or CS in serum containing (20% human serum) M199 growth media for 4 ÷ 24 h in 5% CO₂ air balanced incubator at 37 °C. After treatment with NPs, cells were either imaged live (in HBSS after being washed twice in HBSS) with an inverted light microscope (OEG SP only), or fixed and imaged with a transmission electron microscope (all types of NPs). For electron microscopy purposes cells were fixed according to the protocol described in the following section.

TEM of Biological Specimens Incubated with NPs: HUVECs (1 × 10⁵) grown on porcine gelatin (0.2% in HBSS) precoated 12 well microplate, were incubated with OEG-coated NPs (1 mL, 8.3 nm, in 20% human serum M199 growth media) for 4 h at 37 °C in a humidified 5% CO₂ balanced air incubator. After treatment, cells were washed three times with PBS (1×), then trypsinised (0.75 mL, 0.25% trypsin 0.01% EDTA solution, Sigma-Aldrich) for 5 min at 37 °C in 5% CO₂. The cell suspension was transferred to a plastic tube (1.5 mL, Eppendorf) and centrifuged (2500 rpm, 5 min, 4 °C). The solution was decanted and the cell pellet was redispersed in a main fixative: glutaraldehyde/formaldehyde (3%/4%, in 0.1 M piperazine-1,4-bis(2-ethanesulfonic acid-PIPES buffer, pH 7.2), then incubated for 15 min at room temperature. Cells were centrifuged (2500 rpm, 5 min, 4 °C) and decanted. To the cell pellet a drop of sodium alginate (5% in water) was introduced with a mixture of PIPES buffer (0.5 mL, 0.2 M) and calcium chloride solution (0.5 mL, 0.2 M in water). When the alginate settled (15 min), the supernatant was removed and the embedded cell pellet was transferred into a glass vial and fixed with post fixative: osmium tetroxide (1%, 0.1 M PIPES buffer) for 1 h. The fixed pellet was washed twice with

water (for 5 min) and stained with uranyl acetate (2%, in water) for 20 min. The specimen was washed with 30%, 50%, 70%, and 95% ethanolic solutions for 10 min each, then absolute ethanol for 20 min twice. Dehydrated cells were embedded in TAAB resin (Agar Scientific Ltd.) and polymerised at 60 °C for 24 h. Resin blocks were cut using Leica RM 2255 microtome to obtain ultrathin sections (≈ 100 nm thickness). Sections were deposited on TEM grids and stained with Reynolds lead stain prior to imaging.

Inductively Coupled Plasma: HUVECs (1×10^5) were grown on porcine gelatin (0.2% in HBSS) precoated 12 well microplate and incubated with OEG-coated NPs (1 mL, 8.3 nm) in a 20% human serum M199 media growth) for 4 h at 37 °C in a humidified 5% CO₂ balanced air incubator. After treatment, cells were washed three times with PBS (1 \times) and trypsin solution (0.75 mL, 0.25% trypsin 0.01% EDTA solution, Sigma-Aldrich) was added. HUVECs were incubated for 5 min at 37 °C in 5% CO₂, then PBS (5 mL, 1 \times) was added and the cell suspension was transferred into a plastic tube (15 mL) and centrifuged (2500 rpm, 5 min, 4 °C). The cell pellet was redispersed in PBS (1 mL, 1 \times), counted and transferred into a glass vial. Cells (and NPs) were then digested with aqua regia (9 mL) and the gold content was measured by ICP-AES.

Toxicity Assay: HUVECs (2×10^4) grown on porcine gelatin (0.2% in HBSS) precoated 96 well microplate, were incubated with OEG-coated NPs (200 μ L, 8.3 nm), in a full-serum growth media) for 96 h at 37 °C in a humidified 5% CO₂ balanced air incubator. After treatment, cells were washed twice with HBSS (200 μ L, 1 \times) and stained with Hoechst stain (Invitrogen, 100 μ L of 1 μ g mL⁻¹). The fluorescence was measured at 355 nm excitation and 460 nm emission wavelengths using Fluoroskan Ascent plate reader (Labsystems).

Supporting Information

Supporting Information is available from the Wiley Online Library or from the author.

Acknowledgements

We thank Biomedical Imaging Unit in Southampton General Hospital, and the Nanobiotech facility, Italian Institute of Technology, Genoa for technical support. The University of Southampton (NanoUSRG and Adventure in Research Scheme) and the Royal Society are gratefully acknowledged for funding of this project. AGK thanks the Research Council UK (RCUK) for a Roberts fellowship. DB thanks the University of Southampton and EPSRC for financial support. OLM is supported by HEFCE through a SEPnet lectureship.

- [1] Y. Xia, W. Li, C. M. Copley, J. Chen, X. Xia, Q. Zhang, M. Yang, E. C. Cho, P. K. Brown, *Acc. Chem. Res.* **2011**, DOI: 10.1021/ar200061q.
- [2] W. J. Stark, *Angew. Chem. Int. Ed.* **2011**, *50*, 1242–1258.
- [3] D. A. Giljohann, D. S. Seferos, W. L. Daniel, M. D. Massich, P. C. Patel, C. A. Mirkin, *Angew. Chem. Int. Ed.* **2010**, *49*, 3280–3294.
- [4] X. Huang, S. Neretina, M. A. El-Sayed, *Adv. Mater.* **2009**, *21*, 4880–4910.
- [5] H. Goesmann, C. Feldmann, *Angew. Chem. Int. Ed.* **2010**, *49*, 1362–1395.
- [6] E. Boisselier, D. Astruc, *Chem. Soc. Rev.* **2009**, *38*, 1759–1782.
- [7] Z. Ali, A. Z. Abbasi, F. Zhang, P. Arosio, A. Lascialfari, M. F. Casula, A. Wenk, W. Kreyling, R. Plapper, M. Seidel, R. Niessner, J. Knoll, A. Seubert, W. J. Parak, *Anal. Chem.* **2011**, *83*, 2877–2882.
- [8] V. See, P. Free, Y. Cesbron, P. Nativo, U. Shaheen, D. J. Ringden, D. G. Spiller, D. G. Fernig, M. R. H. White, I. A. Prior, M. Brust, B. Lounis, R. Levy, L. Cathepsin, *ACS Nano* **2009**, *3*, 2461–2468.
- [9] X. Michalet, F. F. Pinaud, L. A. Bentolila, J. M. Tsay, S. Doose, J. J. Li, G. Sundaresan, A. M. Wu, S. S. Gambhir, S. Weiss, *Science* **2005**, *307*, 538–544.
- [10] C. George, D. Dorfs, G. Bertoni, A. Falqui, A. Genovese, T. Pellegrino, A. Roig, A. Quarta, R. Comparelli, M. L. Curri, R. Cingolani, L. Manna, *J. Am. Chem. Soc.* **2011**, *133*, 2205–2217.
- [11] M. A. Phillips, M. L. Granb, N. A. Peppas, *Nano Today* **2010**, *5*, 143–159.
- [12] D. Bartczak, T. Sanchez-Elsner, F. Louafi, T. Millar, A. G. Kanaras, *Small* **2011**, *7*, 388–394.
- [13] B. Kang, M. A. Mackey, M. A. El-Sayed, *J. Am. Chem. Soc.* **2010**, *132*, 1517–1519.
- [14] D. Bartczak, O. L. Muskens, T. Millar, T. Sanchez-Elsner, A. G. Kanaras, *Nano Lett.* **2011**, *11*, 1358–1363.
- [15] Z. Krpetic, P. Nativo, V. See, I. A. Prior, M. Brust, M. Volk, *Nano Lett.* **2010**, *10*, 4549–4554.
- [16] J. Chen, C. Glaus, R. Laforest, Q. Zhang, M. Yang, M. Gidding, M. Welch, Y. Xia, *Small* **2010**, *6*, 811–817.
- [17] S. Lal, S. E. Clare, N. J. Halas, *Acc. Chem. Res.* **2008**, *41*, 1842–1851.
- [18] P. K. Jain, I. H. El-Sayed, M. A. El-Sayed, *Nano Today* **2007**, *2*, 18–29.
- [19] D. F. Moyano, V. M. Rotello, *Langmuir* **2011**, DOI: 10.1021/la2004535.
- [20] P. C. Patel, D. A. Giljohann, W. L. Daniel, D. Zheng, A. E. Prigodich, C. Mirkin, *Bioconj. Chem.* **2010**, *21*, 2250–2256.
- [21] J. H. Lee, K. Lee, S. H. Moon, Y. Lee, T. G. Park, J. Cheon, *Angew. Chem. Int. Ed.* **2009**, *48*, 4174–4179.
- [22] B. Xu, J. H. Gao, *Nano Today* **2009**, *4*, 37–51.
- [23] A. Quarta, A. Ragusa, S. Deka, C. Tortiglione, A. Tino, R. Cingolani, T. Pellegrino, *Langmuir* **2009**, *25*, 12614–12622.
- [24] X. Qian, X. H. Peng, D. O. Ansari, Q. Yin-Goen, G. Z. Chen, D. M. Shin, L. Yang, A. N. Young, M. D. Wang, S. Nie, *Nat. Biotechnol.* **2008**, *26*, 83–90.
- [25] M. Bruchez, M. Moronne, P. Gin, S. Weiss, A. P. Alivisatos, *Science* **1998**, *281*, 2013–2016.
- [26] X. Huang, I. H. El-Sayed, W. Qian, M. A. El-Sayed, *J. Am. Chem. Soc.* **2006**, *128*, 2115–2120.
- [27] R. R. Arvizo, O. R. Miranda, M. A. Thompson, C. M. Pabelick, R. Bhattacharya, J. D. Robertson, V. M. Rotello, Y. S. Prakash, P. Mukherjee, *Nano Lett.* **2010**, *10*, 2543–2548.
- [28] C. Brandenberger, C. Muhlfield, Z. Ali, A. G. Lenz, O. Schmid, W. J. Parak, P. Gehr, B. Rothen-Rutishauser, *Small* **2010**, *6*, 1669–1678.
- [29] M. Liang, I. C. Lin, M. R. Whittaker, R. F. Minchin, M. J. Monteiro, I. Toth, *ACS Nano* **2010**, *4*, 403–413.
- [30] E. C. Cho, L. Au, Q. Zhang, Y. Xia, *Small* **2010**, *6*, 517–522.
- [31] A. M. Alkilany, P. K. Nagaria, C. R. Hexel, T. J. Shaw, C. J. Murphy, M. D. Wyatt, *Small* **2009**, *5*, 701–708.
- [32] P. Nativo, I. A. Prior, M. Brust, *ACS Nano* **2008**, *2*, 1639–1644.
- [33] D. A. Giljohann, D. S. Seferos, P. C. Patel, J. E. Millstone, N. L. Rosi, C. A. Mirkin, *Nano Lett.* **2007**, *7*, 3818–3821.
- [34] B. D. Chithrani, A. A. Ghazani, W. C. W. Chan, *Nano Lett.* **2006**, *6*, 662–668.
- [35] B. D. Chithrani, W. C. W. Chan, *Nano Lett.* **2007**, *7*, 1542–1550.

- [36] A. Verma, O. Uzun, Y. Hu, Y. Hu, H. S. Han, N. Watson, S. Chen, D. J. Irvine, F. Stellacci, *Nat. Mater.* **2008**, *7*, 588–595.
- [37] B. Kim, G. Han, B. J. Toley, C. K. Kim, V. M. Rotello, N. S. Forbes, *Nat. Nanotechnol.* **2010**, *5*, 465–472.
- [38] F. Zhao, Y. Zhao, Y. Liu, X. Chang, C. Chen, Y. Zhao, *Small* **2011**, *7*, 1322–1337.
- [39] L. Y. T. Chou, K. Ming, W. C. W. Chan, *Chem. Soc. Rev.* **2011**, *40*, 233–245.
- [40] A. M. Alkilany, C. J. Murphy, *J. Nanopart. Res.* **2010**, *12*, 2313–2333.
- [41] A. G. Kanaras, F. S. Kamounah, K. Schaumburg, C. Kiely, M. Brust, *Chem. Comm.* **2002**, *20*, 2294–2295.
- [42] D. Bartczak, A. G. Kanaras, *Langmuir* **2010**, *26*, 7072–7077.
- [43] S. D. Perrault, C. Walkey, T. Jennings, H. C. Fischer, W. C. W. Chan, *Nano Lett.* **2009**, *9*, 1909–1915.
- [44] G. L. Ellman, *Arch. Biochem. Biophys.* **1959**, *82*, 70–77.
- [45] P. K. Jain, W. Qian, M. A. El-Sayed, *J. Am. Chem. Soc.* **2006**, *128*, 2426–2433.
- [46] A. S. Urban, M. Fedoruk, M. R. Horton, J. O. Radler, F. D. Stefani, J. Feldmann, *Nano Lett.* **2009**, *9*, 2903–2908.
- [47] J. R. Cole, N. A. Mirin, M. W. Knight, G. P. Goodrich, N. J. Halas, *J. Phys. Chem. C* **2009**, *113*, 12090–12094.
- [48] H. H. Richardson, M. T. Carlson, P. J. Tandler, P. Hernandez, A. O. Govorov, *Nano Lett.* **2009**, *9*, 1139–1146.
- [49] C. Ungureanu, R. Kroes, W. Peterson, T. A. M. Groothuis, F. Ungureanu, H. Janssen, F. W. B. van Leeuwen, R. P. H. Kooyman, S. Manohar, T. G. van Leeuwen, *Nano Lett.* **2011**, *11*, 1887–1894.
- [50] J. Turkevich, P. C. Stevenson, J. Hillier, *Discuss. Faraday Soc.* **1951**, *11*, 55–75.
- [51] B. Nikoobakht, M. A. El-Sayed, *Chem. Mater.* **2003**, *15*, 1957–1962.
- [52] S. J. Oldenburg, R. D. Averitt, S. L. Westcott, N. J. Halas, *Chem. Phys. Lett.* **1998**, *288*, 243–247.

Received: July 13, 2011
Revised: August 25, 2011
Published online: